Gondwana Research 110 (2022) 128–142

Contents lists available at ScienceDirect

Gondwana Research

journal homepage: www.elsevier.com/locate/gr

Global Phanerozoic sea levels from paleogeographic flooding maps

Chloé M. Marcilly [a,*], Trond H. Torsvik [a,b], Clinton P. Conrad [a]

[a] Centre for Earth Evolution and Dynamics (CEED), University of Oslo, 0315 Oslo, Norway
[b] School of Geosciences, University of Witwatersrand, Johannesburg 2050, South Africa

ARTICLE INFO

Article history:
Received 3 January 2022
Revised 22 April 2022
Accepted 20 May 2022
Available online 1 June 2022
Handling Editor: R. D. Nance

Keywords:
Phanerozoic sea level
Paleogeographic reconstructions
Global flooding
Global hypsometry

ABSTRACT

The validity of sea level estimates based on stratigraphic correlations has been debated since the 1990 s as relative sea level curves differ between sites due to local tectonics, different deposition rates and changes in dynamic topography. Here, we offer a new eustatic (global) sea level curve for the past 520 million years (Myrs) based on observations of global flooding. We use paleogeographic reconstructions to measure the area of today's exposed land that was flooded in the past (*modern-land flooding*). We then apply the modern global hypsometric slope to reconstruct the sea level history. We find minimum sea levels (comparable to today's level) towards the end of Pangea (210 Ma) and peak levels (~280 m higher than today) at 80 Ma when Pangea was widely dispersed. A first-order "supercontinent" cycle of 250 million years (Myrs) is recognized but we also document a second-order cycle of 37 Myrs that was previously thought to be undetectable using the hypsometric method. The hypsometric slope is critical for reconstructing past sea levels, and steepening the hypsometric slope during Pangea assembly implies dramatically larger sea level fluctuations. Our new sea level curve shares strong similarities with stratigraphic constraints and correlates with seafloor production proxies throughout the Phanerozoic. Measurements of global flooding represent averages across great continental extents, making them less sensitive than stratigraphic analyses to regional-scale vertical land motion, such as from dynamic topography and hence more reliable for estimating eustatic sea level. This method can also help to identify local deviations caused by regional uplift or subsidence and serves to constrain geodynamic mechanisms for sea level change. Our new sea level reconstruction usefully tracks global variations in Phanerozoic eustatic sea level, but also opens opportunities to estimate such variations in deeper time.

1. Introduction

Sea level and its fluctuations over various timescales are indicators of changes across multiple earth processes, including climatic and tectonic changes as well as time-dependent mantle dynamics. Eustatic or global sea level variations may be driven by changes in the volume of water in the oceans, controlled by the amount of water stored on land in glaciers and groundwater. On timescales of 10 s to 100 s of Myrs, water exchange with Earth's mantle contributes to large sea level fluctuations (Karlsen et al., 2019). Eustatic changes on such timescales also result from plate tectonics and mantle processes that create volcanoes, mid oceanic ridges, and continental orogeny, which vertically deflect the seafloor or change its area (e.g., Conrad, 2013). Stresses associated with mantle flow can also trigger up to a kilometer (km) of dynamically supported topography that affects eustatic sea level as well as coastal (i.e., local) observations of sea level (e.g., Moucha et al., 2008; Conrad and Husson, 2009).

Eustatic sea level changes can be quantified using stratigraphic methods and other paleoenvironmental indicators (e.g., Miller et al., 2005). Fossil corals provide high precision constraints for the past few million years, and indicate rates of sea level rise as high as 40 mm/yr (Lambeck et al., 2014), an order of magnitude higher than Anthropocene-driven changes (~3 mm/yr). In deep time (i.e., > 100 Ma), the number of methods that can be used to reconstruct sea level is limited. They are essentially restricted to methods associated with stratigraphy, which uses fossil markers and sedimentary facies changes to assess the position of the shoreline through time (e.g., Haq & Al-Qahtani, 2005; Haq & Schutter, 2008; Miller et al., 2005, Hardenbol et al., 1998) and plate tectonic reconstructions, which assess changes to the depth and the extent of ocean basins (e.g., Vérard et al., 2015; Conrad, 2013). However, plate tectonic methods require full-plate polygons with age-estimates for the oceanic lithosphere that are mainly synthetic before the Cretaceous.

* Corresponding author.

https://doi.org/10.1016/j.gr.2022.05.011
1342-937X/

Most stratigraphy-based Phanerozoic sea level curves show consistent long-duration fluctuations (Fig. 1) with (1) high (200 to 400 m) sea levels in the early Paleozoic, (2) low (50 to −25 m) sea levels during Pangea times (320–250 Ma), (3) peak sea level in the Late Cretaceous (~250 m at 100–80 Ma) and (4) declining sea levels during Late Cretaceous and Cenozoic times (from 200 m to present-day level). Most variations are within the 200 m range, but some studies yield variations up to 400 m above and 50 m below present-day levels (e.g., Hallam, 1992; Snedden & Liu, 2010, 2011). Although the reported amplitudes of the early Paleozoic and late Mesozoic sea level high-stands vary significantly, the relative consistency of the temporal variations in the different stratigraphic curves suggests that they can place practical constraints on the plate tectonic processes that largely control them. Nevertheless, stratigraphy-based sea level curves have been challenged because they simultaneously measure eustatic sea level change and local uplift or subsidence at the observation location (Kominz et al., 2016; Gurnis, 1993a,b), which can result in over- or under-estimation of global-scale fluctuations. Indeed, the relative sea level assessment is often based on measurement along one or more coastlines and can be affected by the local dynamic topography of the region (Müller et al., 2008; Gurnis et al. 1998; Spasojevic et al., 2008).

Compared to regional stratigraphic observations, global flooding estimates represent averages of sea level change across large areas, making these estimates less sensitive to modification by regional uplift or subsidence. Here, we calculate eustatic sea level change directly from flooding maps using the hypsometric method, which converts continental flooding into changes in sea level using the landmass-specific hypsometric curve (Forney, 1975, Algeo & Wilkinson, 1991; van der Meer et al., 2017; Bond, 1979; Harrison, 1990). This method provides estimates of sea level fluctuations with coarser time-resolution than can be obtained from other methods (e.g., seismic or stratigraphic analysis). However, the hypsometric method holds the significant advantage of being applicable over long periods (>10 Myrs), such as the entire Phanerozoic (Algeo & Wilkinson, 1991). However, this method relies on the accuracy of the flooding estimates. In previous studies, both global continental crust flooding (e.g., Kocsis and Scotese, 2021; Scotese and Golonka, 1992) and 'upper shelf to coastal' flooding (e.g., Ronov, 1994; Smith et al., 2004) are engulfed in the term "flooding". This can lead to confusion and faulty comparisons as these estimates utilize different measurements, and may be subjected differently to corrections for isostatic processes. Furthermore, while the upper limit of the flooded area can usually be identified through time, the lower limit is usually more poorly defined, and needs clarification. We here develop clear terms and definitions for flooding estimates and express the main differences and limitations between two chosen definitions. We also refined flooding estimates based on paleogeographic maps of exposed land (Marcilly et al. 2021). Based on our analyses of flooded land, we here present a new global sea level curve over most of the Phanerozoic with improved accuracy.

2. Methods

2.1. Definition of flooding

The quality of sea level estimates derived from the hypsometric method primarily depends on quantifying the size of flooded land areas over time. This study tests two different definitions of flooding, "*modern-land*" and "*continental*" flooding. "*Modern-land*" flooding is here simply defined as the areal difference between exposed land at a certain time in the past (exposed but moved in time according to the tectonic reconstruction) versus the total land area exposed today. For example, the brown and light blue areas in Fig. 2a are the exposed area today for the reconstructed landmasses, but only the brown areas were exposed at 440 Ma. The light blue areas, therefore, represent land areas flooded at 440 Ma. It should be noted that some of the land flooded today is considered exposed at certain times in the past (pink areas), e.g., within landmasses interior to Gondwana (Fig. 2a) that were juxtaposed in the past. We here consider those areas as shallow areas most likely to be exposed within the 10 Myrs of the map life

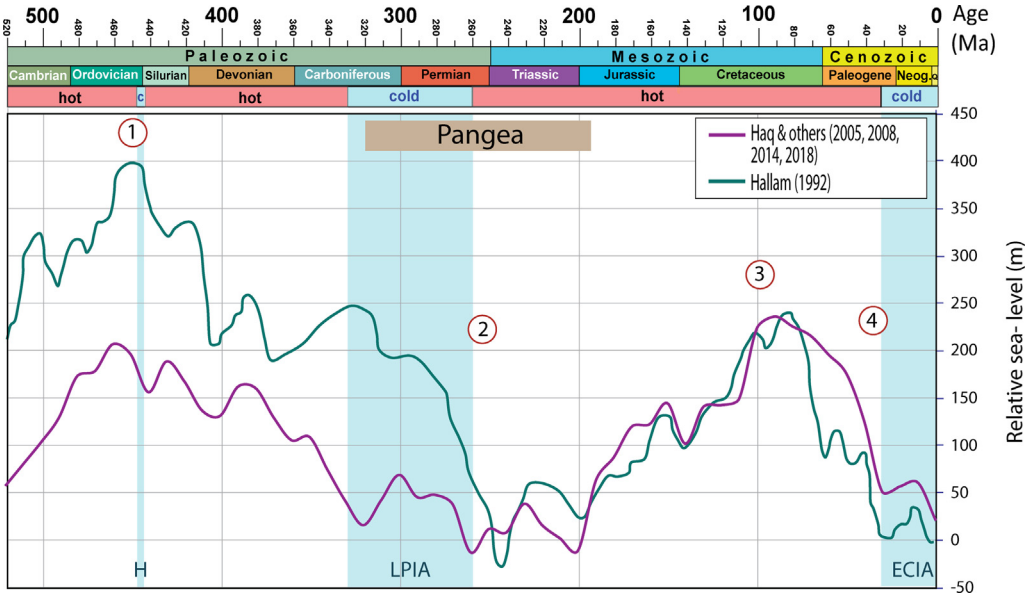

Fig. 1. Timescale with greenhouse (hot) versus icehouse (cold) conditions for the past 520 Myrs and two global sea level curves derived from the use of stratigraphic methods (i.e. Hallam, 1992; Composite curve from: Haq & Al-Qahtani, 2005, Haq & Schutter, 2008, Haq, 2014; 2018). The curve is binned every 10 Myrs to smooth changes in chronostratigraphy (generally less than 4 Myr differences) between studies. Numbers 1 to 4 refer to the description of sea level fluctuations discussed in the text. Bulk Pangea lasted from about 320 to 195 Ma (Veevers, 2004; Torsvik and Cocks, 2017). H, Hirnantian glaciation (end-Ordovician; ~445 Ma); LPIA, Late Paleozoic Ice Age (330–260 Ma); ECIA, End Cenozoic Ice Age (past 30 Myrs). The timing of the main icehouses are extracted from the compilation of Torsvik and Cocks (2016), Fielding et al. (2008), Rocha-Campos et al. (2008), Gaetani et al. (2009), Beerling and Berner (2000), and correspond to periods with large permanent ice-sheets (Scotese et al. 2021).

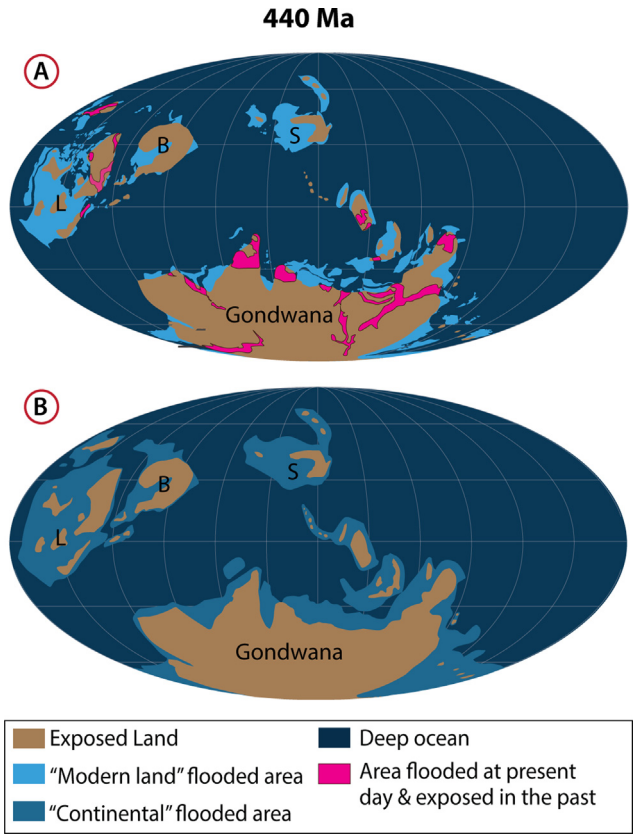

Fig. 2. Plate reconstructions at ~ 440 Ma (early Silurian) with exposed land, deep ocean and **(a)** "*Modern land*" flooded areas (light blue) and exposed land of the past that is currently flooded (pink areas). Our reconstructions assume that small pathways between continents were also exposed in the past, based on lithofacies and fossil distributions over 10 Myr intervals. However, those land areas are not exposed today. **(b)** "*Continental*" flooded area (updated from Marcilly et al., 2021). B, Baltica; L, Laurentia, S, Siberia. (For interpretation of the references to color in this figure legend, the reader is referred to the web version of this article.)

and therefore consider them as exposed. The "*modern-land*" flooding method to estimate global sea levels does not require precise paleogeographic information in terms of absolute latitude and longitude for the continents.

"*Continental*" flooding is here defined as the difference between the area of the continental crust (continental crust polygons modified from Torsvik and Cocks, 2017) and the area of exposed land through time (Fig. 2b). This flooding refers to the inundation of entire continental shelves and includes areas of for example stretched continental crust (pre-breakup extension) along passive margins. Computing the area of flooded continental shelves requires more detailed paleogeographic and plate tectonic knowledge of those areas. Contrarily to the "*modern-land*" flooding estimates, the "*continental*" flooding estimates (Fig. 3a) must be corrected relative to present-day flooding to translate them into relative sea level estimates. The total present-day area of continental crust is estimated to 210.4 mill. km^2 (Cawood et al., 2013), which is almost identical to the areal extent (210.5 mill. km^2) of the continental crust polygon model of Torsvik & Cocks (2017). Based on this continental polygon model, with some revisions, we have mapped out the limit of potential continental crust worldwide for the past 520 Myrs, and the areal extent is listed in Table 1. One simplification in our model is that some areas of exposed oceanic crust today (e.g., Iceland) are incorrectly integrated into the estimates of exposed continental land, leading to an error of 0.08% that is removed from the obtained flooding estimates.

The present-day flooding calculated based on the continental shelves model is ~ 61.5 mill. km^2 which is the difference between present-day area of continental crust (~210.5 mill. km^2) and the exposed land area on Earth (~148.9 mill. km^2). To express the "*continental*" estimates relative to the present, we remove this present-day flooding value (Fig. 3a) from each estimate over the studied period. However, it is worth pointing out that "*continental*" crust estimates through time, as opposed to "*modern-land*" estimates, are often poorly constrained and are the result of a subjective exercise, e.g. how much continental extension took place along a particular rifted margin, how much shortening took place for a specific terrane, and at what time(s) did extension or shortening occur.

The uncertainties linked to the exposed land maps mostly reside in the time-step chosen (i.e 10 Myrs), and some maps, where base-data were lacking, had to be built using extrapolation between the maps ± 10 Myrs around it (Marcilly et al., 2021). It is to be noted that uncertainties are large and numerous for the exposed land reconstructions but nearly impossible to quantify as data become less reliable with time. This is also true when trying to estimate the transition zone between continental and oceanic crust through time (e.g., Torsvik et al. 2009), but this only affects "*continental*" flooding estimates.

2.2. Calculation of sea levels

In order to calculate sea levels from flooding estimates, we used the hypsometric method (Forney, 1975, Bond, 1979) with an estimate of the hypsometric slope that relates continental area to elevation (van der Meer et al., 2017). We consider only one single global and averaged hypsometric slope over Earth's coastal regions, as we aim to calculate global changes in sea level. We therefore do not calculate the slope for each continental landmass separately, unlike previous studies (e.g., Bond (1979); Forney (1975)). To estimate the slope, we used a linear fit over the ETOPO1 global relief model (Amante and Eakins, 2009) corrected for geoid and post-glacial rebound effects (Vérard, 2017). As the elevation for Phanerozoic eustatic fluctuations ranges within a few hundred meters above present sea level, only the low elevation hypsometric curve (i.e., the coastal hypsometry) is required here. The slope of the hypsometric curve is assumed to remain constant in the first few hundred meters (0–200 m) (Forney, 1975; Hallam, 1984). This approximation has been demonstrated as reliable (van der Meer et al. 2017) and enables the following linear relationship:

$$h(t) = F(t) * C \quad (1)$$

F(t) is the time-dependent additional area of continental shelves (in km^2) that will be flooded by sea level rise $h(t)$, while C is the hypsometric slope (in km^2/10^{6}km). In equation (1), the hypsometric curve is used to estimate the eustatic sea level rise that will flood different portions of the continent over time. To use it over the Phanerozoic, we assume that ancient coastal hypsometries were similar to those of the present-day (Forney, 1975). This assumption implies that the shelf margins were identical in slope (albeit located differently across the globe through time).

Models for modern hypsometry suggest different values for C based on whether ice sheets are considered, or if the ice is removed (Amante & Eakins, 2009). A value of 0.0050 km/10^{6}km^2 is estimated by van der Meer et al. (2017) using a model corrected for ice load. However, Vérard (2017) suggests that the slope should additionally be corrected for geoid and post-glacial rebound effects. Furthermore, as we identify variations in sea level that are>200 m (Fig. 1), we recalculated the slope from Vérard (2017) using a linear fit between 0 and 250 m (range of most of the

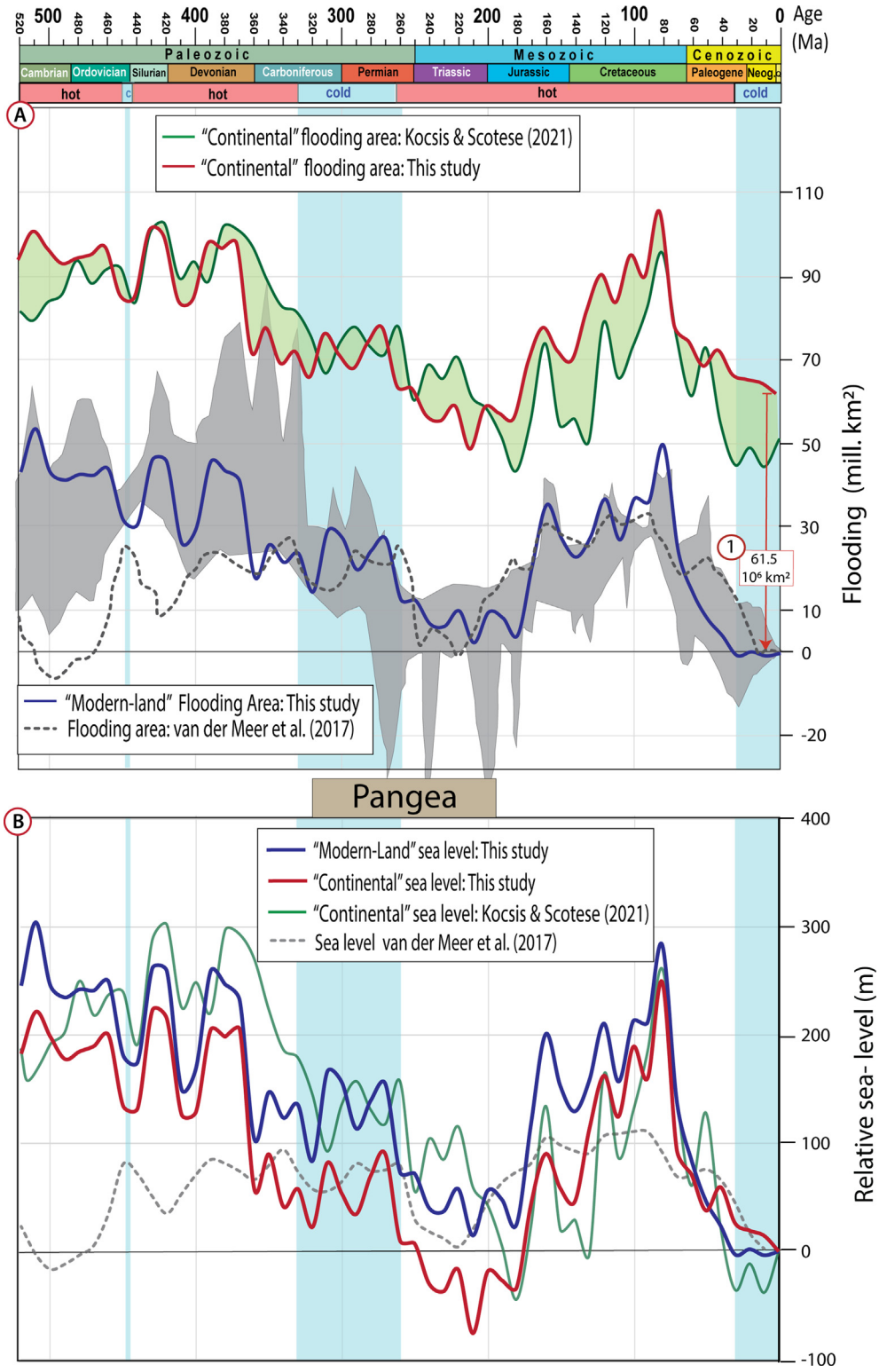

Fig. 3. (a) Time-scale with greenhouse (hot) versus icehouse (cold) conditions for the past 520 Myrs (See Fig. 1 caption for additional details), "*Modern-land*" flooding estimates and our "Continental" flooding estimates (without any corrections) compared with continental flooding estimates of Kocsis & Scotese (2021). The difference between our curve and the one of Kocsis and Scotese (2021) is shaded in green. The offset labeled (1) indicates the correction needed for our "*continental*" estimates to be expressed relative to present. The shaded grey area corresponds to the compilation of flooding areas estimates from different studies compiled by van der Meer et al. (2017). The flooding area from van der Meer et al. (2017; stippled grey line) is based on strontium isotope analysis with correction for weathering processes. **(b)** Estimated "*Modern-land*" (blue curve) and "*Continental*" (red curve) sea levels, compared to sea level reconstructions from Kocsis and Scotese (2021) and van der Meer et al. (2017). (For interpretation of the references to color in this figure legend, the reader is referred to the web version of this article.)

Table 1
Land and flooding areas through time with a 10 Myrs time step, and calculated sea levels for both ''modern-land" and ''continental flooding". The mismatch between modern land and exposed land during 20-0 Ma is linked to many islands that are mapped in the exposed land model.

Age (Ma)	Continental crust 10^6 km^2	Modern land (corrected for Iceland) 10^6 km^2	Exposed land 10^6 km^2	Modern-land flooding Relative 10^6 km^2	Continental flooding 10^6 km^2	Continental flooding relative to present Relative 10^6 km^2	Modern land sea level (C = 0.0057 km/km^2) Relative m	Continental sea level (C = 0.0057 km/km^2) m	Continental sea level (C = 0.0057 km/km^2) Relative m
520	169.40	116.16	75.61	38.67	93.79	32.30	245.84	531.07	182.88
510	167.57	117.83	66.95	49.00	100.62	39.14	304.32	569.78	221.60
500	174.85	118.88	78.29	38.70	96.55	35.07	246.02	546.74	198.55
490	173.28	119.00	80.37	36.75	92.91	31.42	234.97	526.11	177.92
480	172.98	118.79	78.86	38.05	94.13	32.64	242.32	532.99	184.80
470	174.33	119.07	79.29	37.89	95.03	33.55	241.42	538.12	189.93
460	174.49	118.89	77.69	39.32	96.79	35.31	249.49	548.09	199.91
450	175.03	118.97	89.80	27.29	85.23	23.74	181.37	482.61	134.42
440	175.76	118.98	90.86	26.24	84.90	23.41	175.44	480.75	132.56
430	176.61	119.16	75.77	41.51	100.84	39.36	261.91	571.02	222.84
420	176.84	120.27	77.37	41.02	99.47	37.98	259.14	563.24	215.05
410	180.65	120.40	96.75	21.77	83.90	22.41	150.12	475.08	126.89
400	179.80	122.57	95.50	25.19	84.29	22.81	169.48	477.31	129.12
390	177.74	123.00	80.10	41.02	97.65	36.16	259.14	552.93	204.74
380	178.77	122.96	82.21	38.87	96.56	35.08	246.98	546.78	198.59
370	182.78	123.16	85.04	36.24	97.74	36.25	232.06	553.45	205.26
360	179.20	123.03	107.55	13.60	71.65	10.16	103.89	405.71	57.52
350	177.28	123.06	99.92	21.27	77.36	15.88	147.27	438.06	89.87
340	175.28	125.42	106.48	17.07	68.80	7.31	123.49	389.58	41.40
330	176.77	126.16	105.10	19.18	71.67	10.18	135.49	405.81	57.63
320	182.92	129.36	117.44	10.04	65.47	3.99	83.70	370.75	22.56
310	181.44	131.94	105.51	24.55	75.93	14.45	165.88	429.97	81.79
300	181.73	135.57	110.77	22.92	70.96	9.47	156.62	401.80	53.61
290	186.35	135.98	118.78	15.31	67.57	6.08	113.57	382.62	34.43
280	188.33	136.25	114.45	19.92	73.89	12.40	139.68	418.38	70.19
270	189.27	136.39	111.91	22.60	77.36	15.87	154.80	438.04	89.85
260	190.09	136.89	126.82	8.19	63.27	1.78	73.22	358.26	10.07
250	191.39	138.47	128.62	7.98	62.78	1.29	72.03	355.47	7.29
240	190.50	138.51	134.29	2.34	56.20	−5.28	40.09	318.25	−29.94
230	189.81	138.51	134.84	1.80	54.97	−6.52	37.03	311.26	−36.92
220	189.67	138.52	131.18	5.45	58.49	−2.99	57.74	331.21	−16.98
210	186.81	138.42	138.69	−2.15	48.12	−13.36	14.66	272.49	−75.70
200	190.16	139.02	132.04	5.10	58.12	−3.36	55.75	329.12	−19.07
190	190.04	138.86	133.28	3.70	56.76	−4.73	47.81	321.41	−26.78
180	193.00	139.02	137.46	−0.33	55.54	−5.95	25.00	314.49	−33.70
170	190.78	139.55	121.50	16.17	69.28	7.80	118.41	392.31	44.12
160	184.81	140.02	107.39	30.75	77.41	15.93	200.95	438.36	90.17
150	187.16	140.02	115.35	22.31	71.81	10.32	153.19	406.62	58.43
140	189.50	140.02	119.88	19.75	69.62	8.13	129.56	394.22	46.03
130	196.52	140.02	115.04	25.05	81.48	20.00	158.39	461.39	113.20
120	196.24	140.02	106.04	34.86	90.20	28.71	210.77	510.76	162.57
110	199.28	140.02	115.77	25.24	83.52	22.03	157.11	472.92	124.73
100	201.06	140.24	106.18	36.69	94.88	33.39	212.83	537.25	189.07
90	196.37	139.98	106.57	36.04	89.79	28.31	212.00	508.45	160.26
80	199.67	140.95	94.19	49.29	105.47	43.99	283.52	597.25	249.06
70	198.08	141.44	119.99	24.15	78.09	16.60	138.84	442.18	93.99
60	203.90	141.36	129.82	14.20	74.09	12.60	84.63	419.52	71.33
50	205.20	142.36	137.04	8.08	68.16	6.68	46.56	385.97	37.79
40	213.66	143.01	141.67	4.04	71.99	10.51	23.81	407.66	59.47
30	212.73	143.27	146.64	−0.62	66.09	4.60	−2.88	374.24	26.05
20	211.93	144.53	147.05	0.25	64.88	3.39	1.94	367.39	19.20
10	212.60	145.07	148.57	−0.69	64.03	2.55	−3.62	362.58	14.39
0	210.49	146.14	149	−0	61.49	0.00	0.00	348.17	0.00

variations). This results in a value of C = 0.0057 km/10^6km^2, which we use here.

Once the hypsometric slope is chosen, relative sea level fluctuations can be calculated by estimating flooding through time. This is obtained by calculating the difference between the exposed land area and the total land area (i.e., *"continental"* or ''*modern-land*") at a given time. In this way, we estimated the amount of flooded land for the past 520 Myrs in 10 Myrs intervals (Fig. 3a). By applying this flooding value to equation (1), relative sea level can be expressed as:

$$h = \left(L_{total} - L_{Exposed}\right) * C \quad (2)$$

where L_{total} is the total area of land (*"continental"* or *"modern-land"* in km^2), $L_{Exposed}$ (Marcilly et al. 2021) represents the area of exposed land (in km^2), and sea level is expressed relative to present-day (Fig. 3b; Table 1).

Global sea level estimates on 10 to 100 Myrs scales usually need to be adjusted for the isostatic response (Pitman, 1978; Conrad, 2013; van der Meer et al., 2017). Generally, a mantle mass equal to the added water depth is displaced from beneath the oceanic lithosphere (Conrad, 2013), which decreases the sea level change relative to the continents. Since seawater density is ~ 30% of the density of mantle rocks, isostatic compensation of seawater, when fully completed, should cause the observed sea level change to be

only 70% of the changes in water-level rise (Spasojevic and Gurnis, 2012). Isostatic rebound completes within timescales of ~ 10 k years and therefore it is suitable to apply a full isostatic correction for the timescales considered here (>1 Myr). However, our flooding maps (Fig. 2) are derived from a compilation of several local to regional stratigraphic studies that assess the extent of the coastline that we used to draw the exposed land limit. Therefore, those studies already integrate the effect of global isostasy as they measure the eustatic sea level (when compiled globally) and not the water column. For this reason, it is not necessary to adjust our sea level estimates (e.g., equation (2)) to account for isostatic effects. However, the water volume or basin volume changes that are responsible for this isostatically compensated change in eustatic sea level are larger than the observed change (h in equation (2)) by a factor of 1/0.7 = 1.43 (Conrad, 2013; Pitman, 1978).

3. Results and discussion

3.1. Calculated eustatic sea levels

3.1.1. Flooding and sea levels from "Modern-land" flooding

"*Modern-land*" flooding estimates (Fig. 3a) yield early Palaeozoic (520–460 Ma) sea levels that are about 250 m higher than present day levels (Fig. 3b; Table 1). Large reconstructed fluctuations are notable for the Late Ordovician to the Devonian, with a 74 m oscillation in sea level between 460 and 440 Ma, and a 90 m oscillation between 420 and 390 Ma. The drop in sea level around 450 Ma coincides with the Hirnantian glaciation, which likely lasted less than one million years (Torsvik & Cocks, 2017). A more considerable sea level drop (124 m) occurs near the Devonian-Carboniferous boundary at 370–360 Ma (Fig. 3b). This marks the start of a prolonged 100 Myr period of lower sea levels fluctuating around 150 m until 260 Ma, overlapping with the Late Paleozoic Ice Age (LPIA) that lasted from about 330 to 260 Ma. Peak glacial extent, however, occurred between 300 and 290 Ma (Montañez & Poulsen, 2013; Soreghan et al., 2019).

In the late Permian (260 Ma), sea levels dropped by 81 m, followed by a more gentle decrease until reaching the lowest reconstructed value for the entire Phanerozoic at 210 Ma (~14 m). These low sea levels correspond to the time when bulk Pangea may have been centered above TUZO (Fig. 4a), one of the main large low shear-wave velocity provinces (LLSVPs; Garnero et al. 2007, 2016) in the lowermost mantle (today observed beneath Africa). Central Pangea was situated on top of high dynamic topography that may have contributed to the all-time low in global sea levels at 210 Ma (Fig. 4a). A sharp increase in global sea level (~90 m) is recognized between 180 and 160 Ma and occurred during the main and initial break-up phase of Pangea (Torsvik & Cocks, 2017). Peak Phanerozoic sea levels are noticed at around 80 Ma (~283 m) and are followed by a sharp drop in sea levels until the mid-Cenozoic (Fig. 3b, 5a).

3.1.2. Flooding and sea levels from "Continental" flooding

Our "*continental*" flooding estimates (Fig. 3a) are broadly similar to estimates in Kocsis and Scotese (2021), but our model suggests systematically *less* flooding during the Carboniferous and the Triassic, and significantly *more* flooding (averaging 16 mill. km^2) during the Late Jurassic-Cretaceous and parts of the Cenozoic. The discrepancies for the Carboniferous and Triassic (for example) are mostly related to the shelf area around present-day China, where the Kocsis & Scotese (2021) model suggests significantly larger flooded areas than our model (Marcilly et al., 2021), with differences averaging 9 million km^2 and a maximum difference at 360 Ma (nearly 30 million km^2). Kocsis and Scotese (2021) display less present-day continental flooding than is currently observed on Earth (61.5 million km^2). This discrepancy is linked to their choice of definition for the transition from continental to oceanic crust (set at 1400 m isobaths), while our model is based on detailed mapping of the continental-ocean transition zone worldwide using seismic and potential field data (e.g. Torsvik et al. 2009). Kocsis and Scotese (2021) chose to create smaller areas with continental crust along the passive margins compared to our model, explaining the present-day differences.

Continental flooding estimates must be corrected for the present-day value when integrated into equations (1) and (2). The volume of continental crust increased over the Phanerozoic but estimates of the increase in crustal growth differ vividly among different models (2% to 39%; Cawood et al., 2013 and reference therein). Our model considers only the continental area, representing essentially stretched continental crust at passive margins that we here call "shelves", and incorporates negligible, or only minor, additional crustal volumes. For this reason, crustal growth models should not be used to scale our flooding estimates. Instead, we subtracted the modelled present-day flooding (Fig. 3a) from all estimates over the studied period, expressing flooding relative to the present (e.g., Forney, 1975, Bond, 1979, van der Meer et al., 2017 and references therein).

"*Continental*" flooding estimates generally result in lower sea levels (on average −75 m), most notably during Pangea times (Fig. 3b, Table 1), but sea level curves based on "*continental*" and "*modern-land*" flooding estimates are broadly similar with an average sea-level difference of 50 m over the past 520 Myrs.

3.2. Comparison of estimates with other flooding-based sea level curves

Over the past 30 years, numerous estimates of flooding through time have been published (see compilation in van der Meer et al. 2017 based on (Golonka et al., 1994; Ronov,1994; Blakey, 2008; Walker et al., 2002; Scotese, 2016). The overall trends are broadly similar over the Phanerozoic, but there are significant differences in estimated sea levels (grey-shaded background in Fig. 3a).

"*Continental*" flooding-based sea levels calculated here (red curve in Fig. 3b) are mostly within the range of previous estimates but there are clear exceptions during the Hirnantian (~445 Ma) and the Carboniferous (~360–310 Ma) where our reconstructions show lower values than most previous estimates. When calculated with the same hypsometric slope, sea level from the "*continental*" flooding model of Kocsis and Scotese (2021) (green curve in Fig. 3b) implies consistently higher sea levels than our model between 500 and 180 Ma (averaging to 211 m versus 87 m in our model), but lower sea levels during the Early Jurassic and Early Cretaceous (comparable to the present day) (see supplementary material).

"*Modern-land*" calculations represent a better-constrained set of estimates as both the present-day exposed land and the past exposed land are based on physical observations that are used to build the flooding estimates. Our "*modern-land* "flooding and therefore sea level estimates generally plot within the average range from other studies and "*continental*" estimates, except for the Hirnantian and parts of the Carboniferous (Fig. 3). The "*modern-land*" curve is generally higher than the *continental* curve between 180 and 80 Ma.

3.3. "Modern-land" estimates vs stratigraphic and tectonic methods

Our "*modern-land*" sea level curve shows high sea levels in the mid-Cambrian and the Early-Mid-Ordovician, and thus differs significantly from the composite curve from Haq and others, here referred to as the Haq curve (Haq & Al-Qahtani, 2005; Haq and Schutter; 2008, Haq, 2014; 2018), which suggests steadily increas-

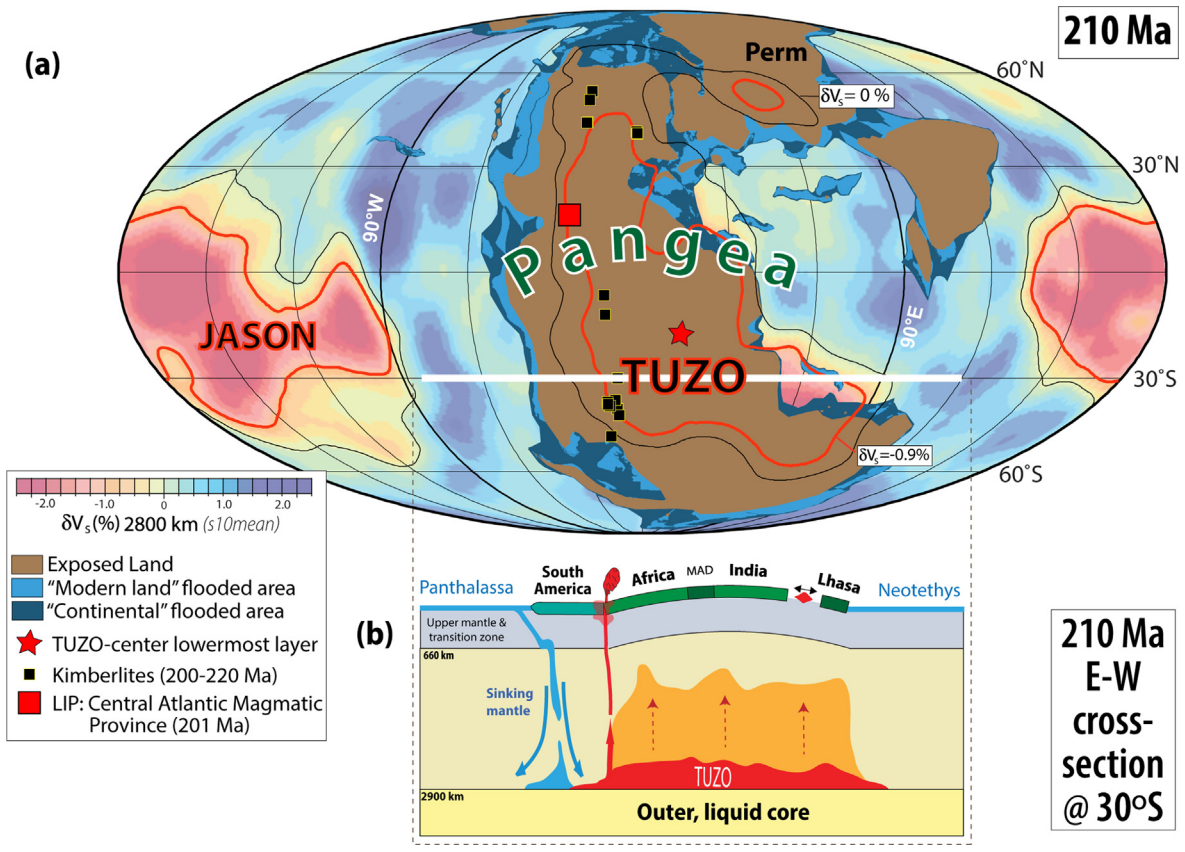

Fig. 4. **(a)** Reconstruction at 210 Ma (in a mantle reference frame; Torsvik & Cocks, 2017) where exposed land (*brown areas*) (Marcilly et al., 2021) and *"Modern land (light blue areas) / Continental (Dark blue areas)"* flooded areas are draped on the *s10mean* tomography model (δV_S%) at 2800 km depth (Doubrovine et al., 2016). Thick red lines are the 0.9% slow contour (largest horizontal gradients in *s10mean*) and the thin black lines are the zero contours. The lowermost mantle is dominated by two large low shear-wave velocity provinces (LLSVPs, Garnero et al. 2007, 2016), named TUZO (beneath Africa) and JASON (beneath the Pacific), which dominate the residual (positive) geoid (Burke et al., 2008; Torsvik et al., 2016). The center of the lowermost TUZO layer is marked by a red star (beneath SW Africa). This juxtaposition assumes that the lower mantle thermochemical piles have remained relatively stable back to 210 Ma (e.g., Torsvik et al. 2010b). At this time, Pangea stretched from pole-to-pole and the bulk of exposed land was centered over TUZO. We estimate some of the lowest sea levels for the Phanerozoic during this time (Fig. 5a). **(b)** 210 Ma east–west cross-section at 30°S from the Panthalassic Ocean to the Neotethys. Surface continents in the cartoon profile of Pangea include S. America, S. Africa, Madagascar (MAD), India and Lhasa, and overlying TUZO, which are warmer but probably also denser and stiffer than the ambient mantle in its lowermost few hundred kilometers (red color). The orange color above TUZO is shown to indicate that the area above TUZO is also warmer than the background mantle, and tends to be overlain by positive dynamic topography anomalies (e.g. Torsvik et al., 2016) as indicated by the "bulged" Pangean lithosphere. A dynamically uplifted Pangea may feature a steeper hypsometric gradient than today's world, lessening Pangean flooding for a given sea level offset (see section 3.4). Between 220 and 200 Ma, plumes sourced from the western margin of TUZO are witnessed by kimberlites and one large igneous province (Central Atlantic Magmatic Province) and older triggering slabs that we relate to subduction along the western margin of the Americas. (For interpretation of the references to color in this figure legend, the reader is referred to the web version of this article.)

ing sea levels until the end Ordovician (Fig. 5a). However, the two curves match reasonably well in trend from the Early Ordovician to the middle Carboniferous. Our curve shows a local low near the End-Ordovician Hirnantian glaciation, very similar to the fluctuations presented by the Haq curve, despite large discrepancies in levels during the early Paleozoic, with on average + 150 m over the peaks at 430 and 390 Ma in our estimates compared to the Haq curve. One of the major differences with the Haq curve is the sharp drop of 150 m that we model between 370 and 350 Ma, whereas the Haq curve suggests a more gradual decrease from 390 to 320 Ma. However, both models reach a low at 320 Ma (Fig. 5a). During the Late Paleozoic, the two curves differ substantially as the Haq curve generally shows much lower sea levels (as much as 90 m), notably near the start of the Pangea assembly. Our curve shows a marked drop in sea level near the end of the LPIA and reaches minimum sea levels at around 210 Ma, whereas the Haq curve models an all-time low between 210 and 200 Ma (Fig. 5a). Contrarily to what is observed at the end-Ordovician glaciation, the peak of the LPIA glaciations (i.e. ~ 300 Ma) does not correspond to a minimum in sea level, either from our method or from stratigraphic methods.

From about 190 Ma (soon after the main Pangea break-up) to 80 Ma, the two curves show gross similarities, and in our estimates, sea levels increased from about 28 m to about 280 m at 80 Ma. Both curves show Phanerozoic peaks in sea levels during the late Cretaceous, but the Haq curve suggests a slightly earlier peak than our reconstructions (i.e. 90 Ma versus 80 Ma). Unlike several other sea level reconstructions (e.g., Hallam, 1992, and Haq and Al-Qahtani, 2005, van der Meer et al. (2017) in Figs. 1 & 5a), our sea level curve does not display any fluctuation during this Cenozoic drop in sea level (Fig. 5a).

van der Meer et al. (2017) flooding estimates, based on an independent method using strontium isotopes, are much lower than our estimates during the early Paleozoic, and the fluctuations seem to occur 10–20 Myrs earlier compared to our reconstruction. Conversely, the Late Paleozoic displays fluctuations and sea levels that compare well with ours. However, from the mid-Jurassic, the strontium-based estimates are once again much lower than both

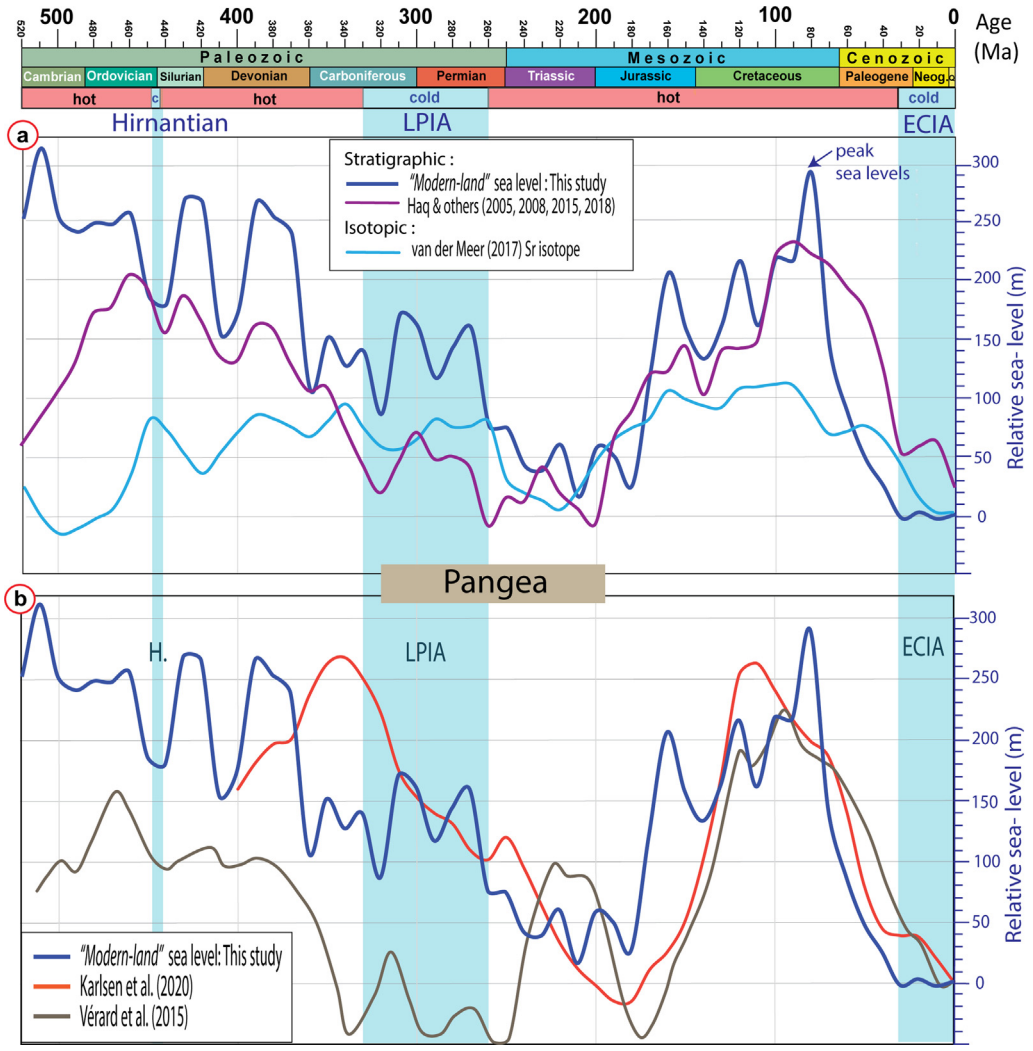

Fig. 5. Time-scale with greenhouse (hot) versus icehouse (cold) conditions for the past 520 Myrs (See Fig. 1 caption for additional details) and "*Modern-land*" sea levels compared with **(a)** the stratigraphically-derived long-term curve from the composite curve of Haq & others (2005, 2008, 2014, 2018) as well as the Sr isotope based estimates from van der Meer et al. (2017)**.** Both curves are binned every 10 Myrs, as is our curve, to facilitate comparisons. **(b)** Comparison to sea level estimates from tectonic models (Karlsen et al., 2020; Vérard et al., 2015).

flooding and stratigraphic methods, even though the global trend is similar for all (Fig. 5a).

Our "modern land" based sea level curve also shows gross similarities with the tectonic-based sea level curves for parts of the Mesozoic and the Cenozoic, but the late Paleozoic curves are markedly different (Fig. 5b). For example, the tectonic-based model of Karlsen et al. (2020) (Fig. 5b) yields very high sea levels (270 m) during the Carboniferous at 340 Ma (just prior to the LPIA), whereas a different tectonic-based model of Vérard et al. (2015) suggests very low sea levels (-40 m). However, tectonic-based sea-level curves are poorly constrained before Pangea (Torsvik et al. 2010), and our flooding-based model, which is not critically dependent on plate reconstructions, suggests intermediate sea levels of about 150 m.

From a global perspective, our "*modern-land*" estimates largely follow stratigraphic models (Fig. 5a) back to the early Mezosoic and only partially agree with tectonic models back to the late Paleozoic (Fig. 5b). However, there is a larger diversity among the tectonic models because tectonic models require full-plate models with ages for the oceanic lithosphere, which can differ significantly, and partly because they account for sea-level changing processes differently (e.g., Karlsen et al. (2019) include water exchange with the mantle while Vérard et al. (2015) do not). The two full-plate models are also fundamentally different. Contrarily, sea level reconstructions based on flooding estimates are either not sensitive or only marginally sensitive to tectonic models based on oceanic crust reconstructions, and thus avoid some of the model uncertainties that can afflict tectonic-based reconstructions. That makes flooding-based sea level reconstructions more reliable, and the close tracking of the stratigraphic and flooding-based curves (Fig. 5a) supports this.

3.4. Sea-levels during Pangea: Effect of changing hypsometric slopes

Assuming a constant hypsometric slope for the 0–250 m elevations for the past 520 Myrs is obviously a simplification. In reality, hypsometric curves change over time due to tectonic and geomorphological processes such as rifting, suturing of landmasses, changing type and age of continental margins, and uplift and peneplation of cratonic interiors (Algeo & Wilkinson, 1991; Gurnis, 1993a, 1993b; Algeo & Seslavinsky, 1995, Bond, 1979). As an example, the mean continental height and crustal thickness should increase during supercontinent formation (e.g., Zhang, 2005), steepening the hypsometric slope (Algeo & Wilkinson, 1991) for perhaps a

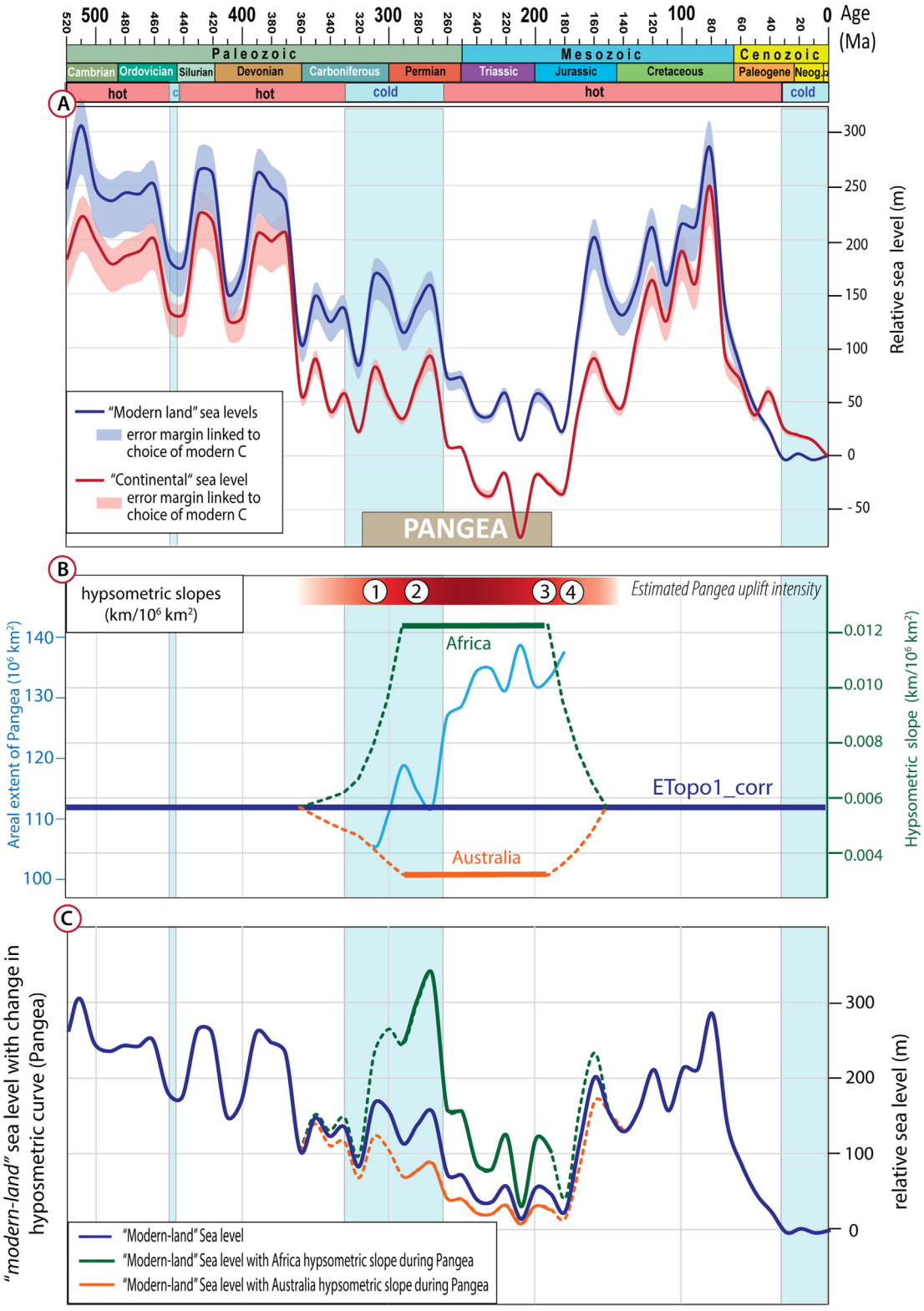

Fig. 6. Time-scale with greenhouse (hot) versus icehouse (cold) conditions for the past 520 Myrs (See Fig. 1 caption for additional details) **(a)** "*modern-land*" and "*continental*" sea levels with error margins linked to the choice of modern day hypsometry from ETOPO1 (applying different corrections for "bed", "ice" in Amante & Eakins (2009) and an additional geoid correction (Vérard 2017)). **(b)** Scenarios tested here with progressive increase and decrease in hypsometric slope during Pangea time. Africa and Australia refer to the slope for the 0–200 m elevation from Harrison et al. (1983) as presented in Algeo & Wilkinson (1991). The choice of time-residency of changes in slope is based on the assembly and break up of Pangea as follows: (1) Initial suturing, Laurussia fused with Gondwana to form Pangea at around 320 Ma, (2) main phase of Pangea assembly and uplift above TUZO, (3) main phase of Pangea break up with the opening of the Central Atlantic ocean at ~ 195 Ma, and (4) break up of Gondwana from 180 to 170 Ma. We also show the areal extent of Pangea (320–195 Ma) in light blue, which includes a late Paleozoic area increase of about 8%, which is mostly related to the merger of Siberia with Pangea. ETOPO1_corr refers to the slope used in our sea level calculations (0.057 km/10^{6}km^2) extracted from Vérard (2017). **(c)** "*Modern-land*" sea level with different choices for hypsometric slope during Pangea time (green curve for Africa and orange for Australia) following the scenarios shown in panel b. (For interpretation of the references to color in this figure legend, the reader is referred to the web version of this article.)

few tens of million years. The increased slope would indicate even higher sea levels to produce the observed flooding that was in place when Pangea formed. Although in many places, periods of large relief are rapidly followed by orogenic collapses and post-collision extension (e.g., Andersen et al., 1991; Stampfli et al., 2013).

Such higher sea levels, however, would have been occurring at a time when we might expect sea level to be depressed. For example, the LPIA glaciation occurred during the first half of Pangea's lifetime (Fig. 6b), and may have lowered eustatic sea level by sequestering water on land. Additionally, we note that Pangea during its zenith assembly (210 Ma) became located above TUZO (Fig. 4a). A persistent upwelling above TUZO would tend to dynamically uplift the continents across supercontinental length scales (Fig. 4b), with Pangea sitting above positive dynamic topography, and on-average low dynamic topography across the surrounding oceans (e.g., Conrad and Husson, 2009). This configuration of relatively deeper oceans would contribute to *lower* sea levels during Pangean time if TUZO has remained fairly stable since Pangea formation (e.g., Torsvik et al. 2014, 2016). Indeed, Conrad (2013) estimated up to ~ 0.5 m/Myr of sea level rise since Pangea breakup as continents move off the dynamic high and the seafloor on average rises. Another sea level-elevating process (e.g., ridge volumes during Pangea that are larger than expected) is thus necessary to offset the sea level depression inherent to the geodynamic positioning of Pangea over broad-scale mantle upwelling (Fig. 4a). Although orogenic events taking place during Pangea formation primarily affected the interior of the continent, and thus may not have significantly influenced coastal hypsometry, we note that positive dynamic topography above TUZO would have uplifted the continent, as it is thought to uplift Africa today (e.g., Lithgow-Bertelloni and Silver, 1998). This dynamic uplift may have contributed to, or even controlled, the steepening of the average hypsometric slope during Pangea formation.

There are no direct records of the variation in the hypsometric curve with time, although modeling studies have attempted to reconstruct such changes (Sømme et al., 2009, Burgess, 2001). However, to account for increased continental height and thickness during Pangea formation, we tested a steepening of the slope (C in Eq. (1)) following supercontinent assembly and uplift (Fig. 6a). The main phase of Pangea assembly started at ~ 320 Ma when Gondwana, Laurussia (including Laurentia and Baltica in Fig. 2) and intervening terranes amalgamated (Torsvik and Cocks, 2017). Pangea constituted ~ 70% of the present-day area of continental crust at that time, but there was a net increase of 8% between 320 and 250 Ma (Fig. 6b).

Algeo and Wilkinson (1991) estimated that Africa, an elevated continent currently positioned above TUZO, has a hypsometric slope that is more than double that of the main continental trend (i.e., average for the globe). Africa is here considered a hypsometric analogue for Pangea, since both are expected to be uplifted continental areas, and we employ its steeper slope of 0.0122 km/10^6km^2 to our calculations of sea level estimates during Pangea (Fig. 6a). During the development of Pangea, we implemented first a small increase in slope from 350 to 320 Ma with values increasing gradually from 0.0057 to 0.0067 km/10^6 km^2 between 350 and 320 Ma. During the most active phase of Pangea, we implemented a sharp but gradual increase of the slope from 0.0067 to 0.0122 km/10^6 km^2 between 320 and 280 Ma (Fig. 6b). However, if the uplift was caused by upwelling above TUZO, it might only have occurred in the central parts of Pangea (Fig. 4a,b), considering that the supercontinent was considerably larger compared to Africa. Therefore, using Africa's hypsometric slope for Pangea might overestimate the slope steepening and thus represents an upper end-value for Pangea's slope.

Table 2
Sea levels calculated using changes in the hypsometric slope. The time interval of change is highlighted in yellow, green for Africa and orange for Australia.

Age	*Scenario of change in hypsometric slope (HS)- AFRICA*	*Modern land sea level with change in HS- AFRICA*	*Scenario of change in hypsometric slope (HS)- AUSTRALIA*	*Modern land sea level with change in HS- AUSTRALIA*
(Ma)	Km/km^2	relative m	Km/km^2	relative m
520	0.0057	245.7	0.0057	245.7
510	0.0057	304.2	0.0057	304.2
500	0.0057	245.9	0.0057	245.9
490	0.0057	234.9	0.0057	234.9
480	0.0057	242.2	0.0057	242.2
470	0.0057	241.3	0.0057	241.3
460	0.0057	249.4	0.0057	249.4
450	0.0057	181.3	0.0057	181.3
440	0.0057	175.4	0.0057	175.4
430	0.0057	261.8	0.0057	261.8
420	0.0057	259.0	0.0057	259.0
410	0.0057	150.1	0.0057	150.1
400	0.0057	169.4	0.0057	169.4
390	0.0057	259.0	0.0057	259.0
380	0.0057	246.9	0.0057	246.9
370	0.0057	232.0	0.0057	232.0
360	0.0057	103.9	0.0057	103.9
350	0.0058	151.5	0.0054	139.5
340	0.0060	130.9	0.0051	111.2
330	0.0062	148.0	0.0049	116.2
320	0.0067	98.5	0.0047	68.8
310	0.0078	229.9	0.0042	122.7
300	0.0095	263.9	0.0038	105.4
290	0.0122	244.0	0.0035	70.1
280	0.0122	300.8	0.0032	79.6
270	0.0122	333.4	0.0032	88.2
260	0.0122	157.7	0.0032	41.7
250	0.0122	155.1	0.0032	41.0
240	0.0122	86.4	0.0032	22.8
230	0.0122	79.7	0.0032	21.1
220	0.0122	124.3	0.0032	32.9
210	0.0122	31.6	0.0032	8.4
200	0.0122	120.1	0.0032	31.8
190	0.0122	103.0	0.0032	27.2
180	0.0095	41.9	0.0036	16.0
170	0.0078	162.1	0.0041	86.1
160	0.0066	232.7	0.0048	169.4
150	0.0057	153.7	0.0057	153.7
140	0.0057	130.0	0.0057	129.6
130	0.0057	158.9	0.0057	158.4
120	0.0057	211.5	0.0057	210.8
110	0.0057	157.6	0.0057	157.1
100	0.0057	213.6	0.0057	212.8
90	0.0057	212.7	0.0057	212.0
80	0.0057	284.5	0.0057	283.5
70	0.0057	139.3	0.0057	138.8
60	0.0057	84.9	0.0057	84.6
50	0.0057	46.7	0.0057	46.6
40	0.0057	23.9	0.0057	23.8
30	0.0057	-2.9	0.0057	-2.9
20	0.0057	1.9	0.0057	1.9
10	0.0057	-3.6	0.0057	-3.6
0	0.0057	0.0	0.0057	0.0

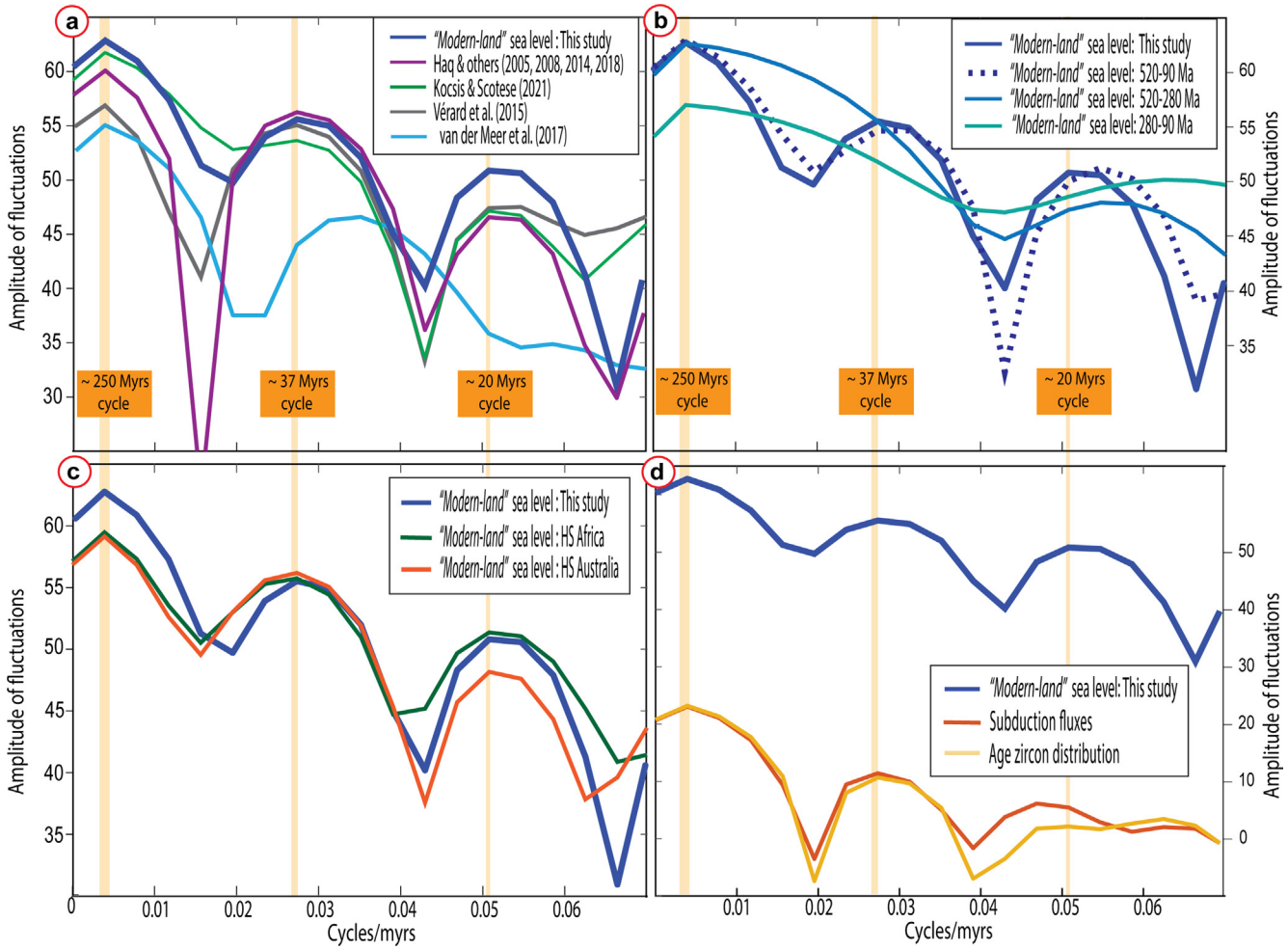

Fig. 7. **(a)** Periodograms derived from stratigraphic (Haq & Al-Qahtani, 2005, Haq & Schutter 2008, Haq, 2014, 2018), tectonic (Vérard et al., 2015) and continental flooding ("Modern-land" sea level from this study; Kocsis & Scotese, 2021) methods. Cycles shorter than 20 Myrs are not considered as the time resolution in our models is 10 Myrs, and estimates used in all the periodograms were binned in 10 Myrs intervals. **(b)** Testing for temporal changes in the cycles. We here test separately the Paleozoic (520–280 Ma) and Mesozoic 280–90 Ma (even if including part of the Permian) as well as the influence of the Cenozoic (compare 520–90 Ma against 520–0 Ma). **(c)** Periodogram showing effects of changed hypsometry during Pangea for both African and Australian slopes. **(d)** Periodogram of proxies for seafloor spreading from Marcilly et al. (2021).

Contrarily, it has been demonstrated that the hypsometric slope in areas of subduction zones is reduced due to sinking slabs pulling the Earth's surface downwards, creating negative dynamic topography (Gurnis, 1993a,b). This was likely also the case for Pangea as the supercontinent was surrounded by subduction zones at several stages of its assembly (Torsvik and Cocks, 2017). Therefore, instead of creating a steepening of the gradient, the development of subduction zones may have instead created a flattening in the gradient. (Gurnis, 1993b) estimated the hypsometric gradient for low-lying (0–200 m) areas near subduction to be close to the value proposed by van der Meer et al. (2017) (0.005 km/10^6km^2) and therefore should not produce significant changes.

To test the hypothesis of a flattened gradient even further, we also applied a flattened gradient of 0.0032 km/10^6 km^2, corresponding to the present-day value for low-lying Australia (Algeo & Wilkinson, 1991) (Fig. 6 b, supplementary material).

After changing the slope of the hypsometric curve from 0.0057 to a gradual increase until 0.0122 km/10^6km^2 (Africa slope, Fig. 6b), *"modern-land"* sea levels rose by + 59 m on average throughout the main uplift period with a maximum increase of + 78 m at 270 Ma compared to an unchanging slope (Fig. 6b & Table 2). Major differences reside in the intensification of large peaks in sea level at 300 and 270 Ma, and minor changes around 220 and 200 Ma increase smaller peaks in sea level. When applying the smaller Australian slope (Fig. 6b), the changes are also initially significant. Indeed, during the maximum decrease of the slope at 270 Ma, the reduction of the peak reaches −66 m (Fig. 6c). These observations suggest that the method used here is highly sensitive to the choice of the hypsometric slope. Such changes can be significant, notably during the end of the Pangea assembly when the hypsometric slope could have reached a maximum. At this period, a substantial discrepancy with other curves arises between our estimates and reference levels (Figs. 1, 5 and 6a, c). Therefore, our use of a fixed slope of 0.0057 km/10^6 km^2 during the Phanerozoic may cause us to underestimate the magnitude of sea-level fluctuations for periods with a steeper slope, or to overestimate them for periods when the hypsometry is flatter. This could potentially explain some of the observed discrepancies with stratigraphic methods (Fig. 5a).

3.5. Cyclicity

In order to identify the cyclicity of sea level changes, we computed the Discrete Fourier Transform (DFT) of the variable sea levels using a fast Fourier transform (FFT) algorithm. As our sea level reconstructions are based on flooding estimates in 10 Myr intervals, only sea level fluctuations ~ 20 Myr or longer can be considered. Fig. 7a displays a significant peak at 250 Myrs, which corresponds to a supercontinent cycle, and this is qualitatively visible by the high sea levels before and after Pangea (Fig. 6a). This ~ 250

Myr first-order peak is generally visible for several other sea level curves (peridograms computed also after binning in 10 Myr intervals, Fig. 7a), as are some shorter-period, second-order cycles.

It has previously been assumed that the hypsometric method is limited to first-order approximations (Hallam, 1984); however, our reconstructions include both first and second-order cycles. Indeed, two smaller peaks are visible in the periodogram but with smaller intensity, and these are second-order cycles (5–50 Myrs) at about 37 and 20 Myrs per cycle (Fig. 7a). These second-order cycles can be observed with ~ 37 Myrs intervals from 510 to 270 Ma and from 200 to 160 Ma. Between 350 and 300 Ma, 270–200 Ma, and 130–80 Ma, cycles are shorter and about 20 Myrs in duration (Fig. 6a). Most other curves considered, computed using a variety of methods, also show similar second-order periodicity (Fig. 7a).

To identify the temporal changes in these cycles we ran the spectral analysis for the Paleozoic and Mesozoic separately (Fig. 7b). Due to the shorter time window, the first order and second order cycles become less clearly identifiable. However, there is still significant power for the longer second order cycles (~37 Myr) during the Paleozoic, while some of the power shifts toward shorter second order cycles during the Mesozoic (Fig. 7b). We additionally analysed the Phanerozoic without the Cenozoic (90–520 Myr), a period without second order fluctuations in our reconstruction. For this case, the peak showing ~ 37 Myr second order cycles becomes sharper and the ~ 20 Myrs cycles peak is displaced towards shorter cycles (Fig. 7b). This suggests that the ~ 20 Myrs cycle may be an artefact linked to the 10 Myrs time step used in our reconstructions. Indeed no shorter cycle than 20 Myrs should be identifiable, as it would be composed of less than 2 points.

A second order cycle with a ~ 37 Myr cycle is thus a recurring strong signal through most of the Phanerozoic (Fig. 7b). We find that this cycle is mostly unchanged by hypsometry, although it becomes more defined and reaches higher power if the hypsometric slope is steeper during Pangea (Fig. 7c). Interestingly, Boulila et al. (2018) also observed cycles with this duration (~36 Myrs), and attributed them to astronomical processes. In particular, they propose that vertical and radial motions of the solar system could induce long-term climatic variations that modulate the ice sheets. To look for a tectonic driver of this cyclicity, we ran the same spectral analysis on two independent datasets from Marcilly et al. (2021) that provide proxies for seafloor spreading (i.e subduction fluxes and age-zircon distributions). This analysis (Fig. 7d) shows a clearly identifiable supercontinental cycle of 250 Myrs, but also tectonic cycles at ~ 37 Myrs. This suggests that tectonic processes may be the source of those second order cycles.

Guillaume et al. (2016) discussed the difficulty for eustatic charts to constrain second order eustatic fluctuations because coastline observations also measure vertical ground motion, due to tectonics or dynamic topography. Furthermore, their analysis of the Permian and Triassic argues that neither tectonic nor glacio-eustatic processes can explain the rates of eustatic change implied by second order cycles during this period. Nevertheless, we have identified a robust second order fluctuation across the Phanerozoic (Fig. 7). This is possible despite Guillaume et al.'s (2016) concerns because our paleogeographic method averages across all coastlines, and therefore is less sensitive to particular tectonic events in any one location.

Furthermore, our identification of a ~ 37 Myr second order cycle (Fig. 7) arises from an analysis of the entire Phanerozoic record, and not just a particular portion of it (e.g., Permian-Triassic). We do observe a correlation with global-scale tectonic indicators (e.g., Fig. 7d and Fig. 8b), but this correlation is more easily explained by tectonic processes generating eustatic change (a global sea level offset), instead of coastline uplift and

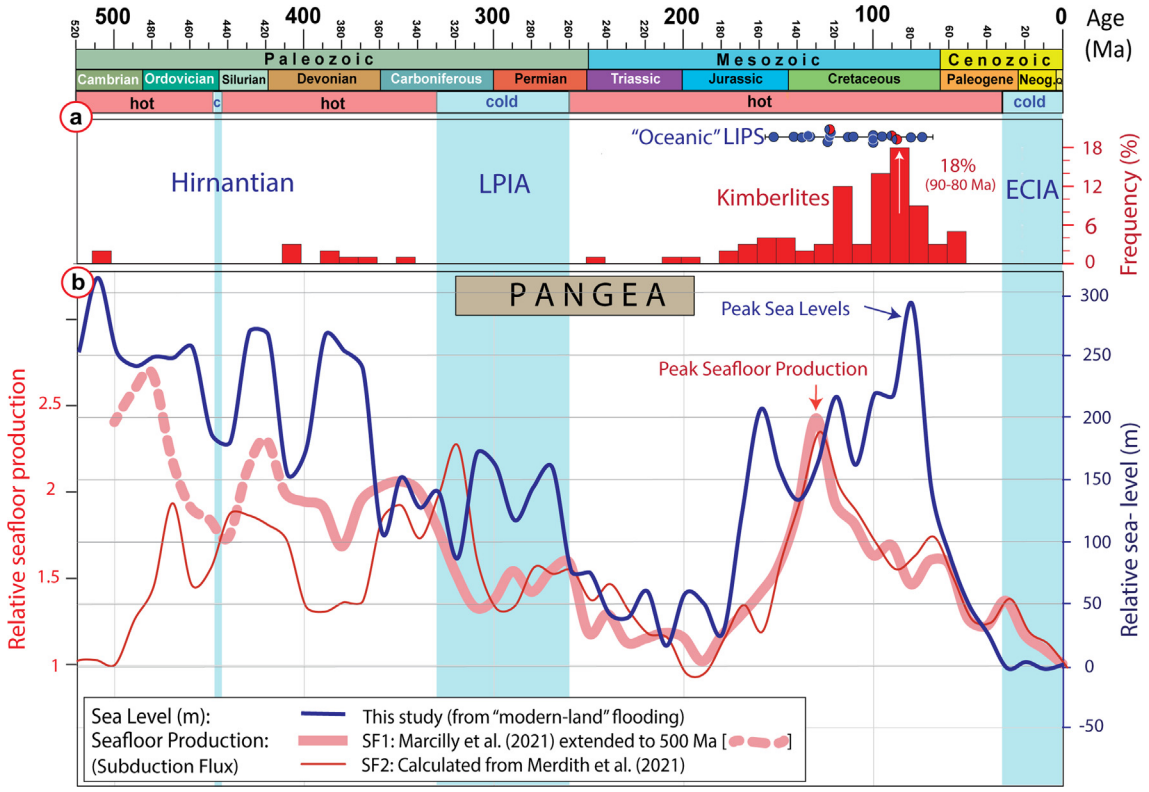

Fig. 8. **(a)** Time-scale, greenhouse (hot) vs. icehouse (cold) (See Fig. 1 caption for additional details), kimberlite frequencies for the past 520 Myrs (10 Myr bins), and preserved "oceanic" large igneous provinces (LIPs). The blue dots represent oceanic LIPs and shared blue/red dots represent continental and oceanic LIPs. **(b)** "*Modern-land*" sea level calculated from flooding maps (this study) compared to two proxies for relative seafloor production calculated from the subduction flux of full-plate models: SF1 from Marcilly et al. (2021) extended from 410 to 500 Ma.; SF2 calculated from the full-plate model of Merdith et al. (2021). (For interpretation of the references to color in this figure legend, the reader is referred to the web version of this article.)

subsidence, which would need to be globally-coherent to explain the observed changes in global flooding.

3.6. Drivers of sea level changes

3.6.1. Seafloor production

Beyond comparing to other observations of sea level change, the credibility of our flooding-based sea level reconstruction can be augmented by a comparison to predictions of sea level change based on possible driving mechanisms. Past sea level variations are dominantly linked to changes in the volume of mid-ocean ridges, which can be computed from global full-plate models (e.g., Müller et al. 2008; Karlsen et al. 2020). However, such models require reconstructions of seafloor ages for past times, and the reconstruction uncertainty, defined by the fraction of the Earth's lithosphere lost to subduction, reaches 60% by 150 Ma (Torsvik et al., 2010a). Alternatively, trends in ridge volume change, which directly impact sea level (e.g., Gaffin, 1987), can be roughly estimated from changes in seafloor production rates (e.g., Vail et al, 1977, Müller et al., 2008; Conrad, 2013). On a planet that is not shrinking or expanding, the rate of seafloor production should approximate the subduction flux. The latter can be estimated with higher confidence, as knowledge of the location of ridges in the distant past is highly limited. Therefore, we here consider subduction flux as a proxy for seafloor production rate, but subduction flux estimates should be treated with great caution prior to the assembly of Pangea.

The subduction flux curve, here named SF1, is that of Marcilly et al. (2021) but extended from 410 to 500 Ma using a full-plate global model that is largely based on two regional models detailed in Domeier (2016, 2018). For the past 300 Myrs, SF1 grossly matches subduction flux estimates from the full plate model of Meredith et al. (2021) (here named SF2), but before that time they generally show large discrepancies (Fig. 8b). SF1 and SF2 are essentially based on the same databases but with the continents, notably for the Paleozoic, located to very different longitudes. This difference leads to very different subduction flux estimates.

Although the oceanic areas of full-plate models are largely synthetic for the entire Paleozoic and parts of the Mesozoic, the SF1 curve, which is based on a full-plate model with calibrated longitudes (Torsvik et al. 2014; Marcilly et al. 2021), is characterized by a general pattern of decreasing seafloor production from 490 to 190 Ma and is grossly similar to our reconstructed sea levels (Fig. 8b). The SF1 curve shows local minima's during the Hirnantian and the LPIA, but the lowest seafloor production and sea levels are observed in the Early Mesozoic. From about 180–190 Ma, estimated sea levels and seafloor production are rising, but seafloor production rates peak at 120–130 Ma and about 40 Myrs before the sea level peak at 80 Ma. We do expect sea level rise to lag behind an increase in spreading rates, perhaps by several tens of Myr given that this is the timescale for seafloor at ridges to slowly fill the oceanic basins with shallower seafloor (Conrad, 2013). We note, however, that significant sea level rise also occurred even earlier, with a rapid rise completed by ~ 160 Ma, and thus before the major increase in seafloor production (Fig. 8b). Here we note that the emplacement of voluminous oceanic Large Igneous Provinces (LIPs) began even before the mid-late Cretaceous (e.g., the Ontong Java plateau at 125 Ma; Ernst, 2014) and may have contributed to or overprinted the sea level peak as discussed below.

3.6.2. Oceanic LIP emplacement

The oldest and youngest preserved oceanic LIPs are 155 Ma (Argo) and 73 Ma (Sierra Leone), respectively (e.g., Torsvik et al., 2021; their *Table 16.2*). In this 82 Myr period there are 22 known LIPs, including 16 oceanic, three with mixed oceanic and continental affinity, and three of continental origin (Svensen et al., 2018; Torsvik et al., 2021). Therefore, the oceanic and "mixed" LIPs represent 86% of all LIP activity from the Late Jurassic to the Late Cretaceous.

The emplacement of oceanic LIPs adds large volumes of basalt to the seafloor, leading to perturbations of global sea level. LIP emplacement may possibly explain the temporal offset between the prominent peaks in seafloor production and sea level (Fig. 8b) due to the pulse-like nature of LIP emplacement. Although the sea level impact of a LIP is challenging to assess due to volume uncertainties (Mills et al., 2014), a ~ 45 m rise between 120 and 80 Ma has been suggested from LIP emplacement models (Wright et al., 2020), while other authors have suggested larger contributions from LIP activity (e.g., Conrad, 2013). This may explain a large fraction of the ~ 70 m rise between 90 and 80 Ma (Fig. 8b), especially since our sea level peak aligns with the peak in LIP activity at ~ 85 Ma as indicated by kimberlites (Fig. 8a).

Due to subduction, there are no traces of *in-situ* oceanic LIPs prior to the Late Jurassic, but similar perturbations in nature and scale may have occurred in deeper time. Such perturbations can potentially explain mismatches and offsets between seafloor production from the plate tectonic model used here and sea level fluctuations from flooding estimates in the Paleozoic. LIPs represent catastrophic melting of the upper mantle, primarily sourced by mantle plumes from the lowermost mantle, but kimberlites (Fig. 4b) are another surface manifestation of those plumes (e.g., Torsvik et al. 2010b; Torsvik et al., 2021). Kimberlites are exclusively found on the continents and will therefore *not* contribute to global sea level changes. However, they provide essential constraints on the plume activity during Earth history. It is well known that the frequency of kimberlite volcanism was high in the Cretaceous (Torsvik et al. 2010b), in concert with LIP emplacement (Fig. 8a). In particular, a rise in kimberlite plume activity is observed from the mid-Jurassic, with a pronounced peak between 120 and 110 Ma (Fig. 8a). Still, the prominent peak, representing 15% of all known kimberlites for the past 520 Myrs, is observed between 90 and 80 Ma, and coincides with the main rise shown by most sea level curves (Fig. 8a, b). The period of intense kimberlite plume activity corresponds to the age range of major ocean LIP volcanism [i.e. the Caribbean-Colombian (90 Ma) and Madagascar events (87 Ma)], and the accumulated LIP volumes may have peaked at this time. Since the Late Cretaceous, LIP and kimberlite activity has been significantly low, with the last oceanic LIP emplaced around 82 Myrs ago (Torsvik et al., 2021). Since then, seafloor production and sea level curves show a similar decreasing pattern (Fig. 8b). Today, Earth is experiencing its lowest seafloor production and sea levels compared to the entire Phanerozoic (past 541 Myr) as also noticed by van der Meer et al. (2017) using an independent model based on strontium isotope ratios.

It is perhaps also worth noting two other periods with high kimberlite activity. First, we note that the Cretaceous peak in activity actually began in the mid-Jurassic (Fig. 8a). If LIP activity also increased in concert with the kimberlites, it may have helped to drive the mid-Jurassic sea level rise that slightly preceded the early Cretaceous increase in seafloor production (Fig. 8b). Note that LIPs emplaced during the mid-Jurassic would have been subducted by now, because the oldest seafloor is only 180 Myr old. Second, we note that the Devonian is associated with a relatively high number of kimberlites (42% of all Paleozoic occurrences) and sea levels were high between 390 and 380 Ma. Conversely, seafloor production curves show a low in this time interval (SF1 and SF2 in Fig. 8b), but seafloor production estimates must be considered with great caution for most of Paleozoic.

4. Concluding remarks

Based on global flooding maps with a constant hypsometric slope (0.0057 km/10^6km^2) we have calculated new sea level curves for the past 520 Myrs using two different definitions of flooding. However, we consider the *"modern-land"* sea level curve, which measures changes in the area of exposed land, to be more reliable and objective than the *"continental"* curve for which changes to the area of flooded continental crust cannot be expressed with high confidence.

Our two definitions of flooding only lead to an average difference of 50 m over the past 520 Ma. However, changes in the assumed value of the hypsometric slope can lead to significantly higher differences in calculated sea levels. Our hypothesis that the Pangean hypsometric slope was steeper as a result of positive dynamic topography implies significantly elevated sea level highstands. For example, a 154 m high-stand at 270 Ma grows to 333 m if we assume a steeper hypsometric slope for Pangea. However, such exercises must be treated cautiously, especially since Pangea may have assembled over elevated dynamic topography that was theoretically associated with low eustatic sea levels. Indeed, we calculate minimum sea levels at 230 Ma, in the latter part of Pangea's lifespan, and about 30 Myrs after the demise of the late Paleozoic ice age. At this time, Pangea was at its largest and centered above the TUZO LLSVP, assuming that the LLSVPs have remained semi-stable since Pangea formed.

Except for the Early Paleozoic, our sea level reconstructions are grossly similar to the stratigraphic-based Haq curves with a Pearson correlation coefficient of 0.68 (*"modern-land"* reconstruction) and 0.79 (*"continental"* reconstruction) for the past 470 Myrs. This suggests that global flooding maps, at least to first order but also probably second order, are useful for determining eustatic sea levels compared to stratigraphic methods. However, with sea level reconstructions based on tectonic models, the comparison is less favourable, especially in the distant past. One reason behind this discrepancy is that such tectonic-based reconstructions require seafloor reconstructions (full-plate models) that are increasingly uncertain in deep time.

Our sea level curve is grossly similar to proxies for temporal changes to seafloor production rates, such as the subduction flux of recent plate tectonic reconstructions, which result in similar first and second order cycles. This link between the primary mechanism for eustatic sea level change (changes in the volume of the mid-ocean ridges) and sea level change inferred from flooding estimates further strengthens the case for the reliability of the paleogeographic methods for reconstructing sea level. Because such models represent averages over large areas of the earth, they are less sensitive to regional uplift or subsidence events (e.g., from dynamic topography and local tectonics) compared to stratigraphic methods, which are usually made at specific locations. Paleogeography thus presents a useful constraint on eustatic (global) sea level change that can be used to deduce the geodynamic mechanisms that drive sea level change (e.g., ridge volume changes or LIP emplacement). Paleogeography may also prove useful for identifying regional uplift or subsidence events where local observations of sea level, such as from stratigraphy, deviate significantly from the eustatic curve.

CRediT authorship contribution statement

Chloé M. Marcilly: Conceptualization, Methodology, Software, Investigation, Formal analysis, Writing – original draft, Visualization, Data curation. **Trond H. Torsvik:** Conceptualization, Supervision, Software, Investigation, Formal analysis, Writing – review & editing, Data curation. **Clinton P. Conrad:** Investigation, Supervision, Resources, Writing – review & editing.

Declaration of Competing Interest

The authors declare that they have no known competing financial interests or personal relationships that could have appeared to influence the work reported in this paper.

Acknowledgments

We acknowledge financial support from the Research Council of Norway (RCN), through its Centres of Excellence funding scheme, project 223272 (CEED), and 288449 to CPC (MAGPIE project). We thank Michelle Kominz, Douwe van der Meer and Christian Vérard as well as one anonymous reviewer for helpful comments that improved the manuscript.

Appendix A. Supplementary data

Supplementary data to this article can be found online at https://doi.org/10.1016/j.gr.2022.05.011.

References

Algeo, T.J., Wilkinson, B.H., 1991. Modern and ancient continental hypsometries. J. Geol. Soc. Lond 148 (4), 643–653.
Algeo, T.J., Seslavinsky, K.B., 1995. The Paleozoic world; continental flooding, hypsometry, and sea level. Am. J. Sci. 295 (7), 787–822. https://doi.org/10.2475/ajs.295.7.787.
Amante, C., Eakins, B.W., (2009). ETOPO1 1 Arc-Minute Global Relief Model: Procedures, Data Sources, and Analysis. NOAA Tech. Memo. NESDIS NGDC-24. http://dx.doi.org/ 10.7289/V5C8276M.
Andersen, T.B., Jamtveit, B., Dewey, J.F., Swensson, E., 1991. Subduction and eduction of continental crust: Major mechanisms during continent-continent collision and orogenic extensional collapse, a model based on the south Norwegian Caledonides. Terra Nova 3 (3), 303–310.
Beerling, D.J., Berner, R.A., 2000. Impact of a Permo-Carboniferous high O2 event on the terrestrial carbon cycle. Proceedings of the National Academy of Sciences 97 (23), 12428–12432.
Blakey, R.C., 2008. Gondwana paleogeography from assembly to break-up—A 500 my odyssey. Geol. Soc. Am. Special Paper 441, 1–28.
Bond, G.C., 1979. Evidence of some uplifts of large magnitude in continental platforms. Tectonophysics 61, 285–305.
Boulila, S., Laskar, J., Haq, B.U., Galbrun, B., Hara, N., 2018. Long-term cyclicities in Phanerozoic sea-level sedimentary record and their potential drivers. Global and Planet. Change 165, 128–136.
Burke, K., Steinberger, B., Torsvik, T.H., Smethurst, M.A., 2008. Plume Generation Zones at the margins of Large Low Shear Velocity Provinces on the Core-Mantle Boundary. Earth Planet. Sci. 265 (1-2), 49–60.
Burgess, P.M., 2001. Modeling carbonate sequence development without relative sea-level oscillations. Geology 29 (12), 1127–1130.
Cawood, P.A., Hawkesworth, C.J., Dhuime, B., 2013. The continental record and the generation of continental crust. Bulletin 125 (1-2), 14–32.
Conrad, C.P., 2013. The solid Earth's influence on sea level. Geol. Soc. Am. Bull. 125 (7-8), 1027–1052. https://doi.org/10.1130/B30764.1.
Conrad, C.P., Husson, L., 2009. influence of dynamic topography on sea level and its rate of change. lithosphere 1 (2), 110–120. https://doi.org/10.1130/l32.1.
Domeier, M., 2016. A plate tectonic scenario for the Iapetus and Rheic Oceans. Gond. Res. 36, 275–295. https://doi.org/10.1016/j.gr.2015.08.003.
Domeier, M., 2018. Early Paleozoic tectonics of Asia: towards a full-plate model. Geosci. Front. 9 (3), 789–862. https://doi.org/10.1016/j.gsf.2017.11.012.
Doubrovine, P.V., Steinberger, B., Torsvik, T.H., 2016. A failure to reject: Testing the correlation between large igneous provinces and deep mantle structures with EDF statistics. Geochem., Geophys., Geosys. 17 (3), 1130–1163.
Ernst, R.E., 2014. Large igneous provinces. Cambridge University Press.
Fielding, C.R., Frank, T.D., Isbell, J.L. (Eds.), 2008. Resolving the Late Paleozoic ice age in time and space, Vol. 441. Geological Society of America.
Forney, G.G., 1975. Permo-Triassic Sea level change. J. Geol. 83 (6), 773–779.
Gaetani, M., Angiolini, L., Ueno, K., Nicora, A., Stephenson, M.H., Sciunnach, D., Rettori, R., Price, G.D., Sabouri, J., 2009. Pennsylvanian-Early Triassic stratigraphy in the Alborz Mountains (Iran). Geological Society, London, Special Publications 312 (1), 79–128.
Gaffin, S., 1987. Ridge volume dependence on seafloor generation rate and inversion using long term sea level change. Am. J. Sci. 287 (6), 596–611.

Garnero, E.J., Lay, T., McNamara, A., 2007. Implications of lower mantle structural heterogeneity for existence and nature of whole mantle plumes. Geol. Soc. Am. Special Paper 430, 79–102. https://doi.org/10.1130/2007. 2430(05).
Garnero, E.J., McNamara, A.K., Shim, S.-H., 2016. Continent-sized anomalous zones with low seismic velocity at the base of Earth's mantle. Nature Geosci. 9 (7), 481–489.
Golonka, J. R., Ross, M. I., & Scotese, C. R. (1994). Phanerozoic paleogeographic and paleoclimatic modeling maps.
Guillaume, B., Pochat, S., Monteux, J., Husson, L., Choblet, G., 2016. Can eustatic charts go beyond first order? Insights from the Permian-Triassic. Lithosphere 8 (5), 505–518.
Gurnis, M., 1993a. Phanerozoic marine inundation of continents driven by dynamic topography above subducting slabs. Nature 364 (6438), 589–593.
Gurnis, M., 1993b. Depressed continental hypsometry behind oceanic trenches - a clue to subduction controls on sea-level change. Geology 21 (1), 29–32. https://doi.org/10.1130/0091-7613(1993)021<0029:dchbot>2.3.co;2.
Gurnis, M., Müller, R.D., Moresi, L., 1998. Cretaceous vertical motion of Australia and the AustralianAntarctic discordance. Science 279 (5356), 1499–1504.
Hallam, A., 1984. Pre-Quaternary sea level changes. Annu. Rev. Earth Planet. Sci. 12 (1), 205–243. https://doi.org/10.1146/annurev.ea.12.050184.001225.
Hallam, A., 1992. Phanerozoic sea level changes. Columbia University Press.
Hardenbol, J., Thierry, J., Farley, M.B., Jacquin, T., de Graciansky, P.-C., Vail, P.R., 1998. Mesozoic and Cenozoic sequence stratigraphy of European basins. SEPM Spec. Publ. 60, 3–13.
Harrison, C. G. A., 1990, Long term eustasy and epeirogeny in continents, in Sea Level Change: U.S. National Research Council Geophysics study Committee (Washington D.C.), p. 141-158.
Haq, B.U., Al-Qahtani, A.M., 2005. Phanerozoic cycles of sea level change on the Arabian Platform. GeoArabia 10 (2), 127–160.
Haq, B.U., Schutter, S.R., 2008. A chronology of Paleozoic sea level changes. Science 322 (5898), 64–68.
Haq, B.U., 2014. Cretaceous eustasy revisited. Global and Planet.change 113, 44–58.
Haq, B., 2018. Triassic Eustatic Variations Reexamined. Triassic eustatic variations reexamined. Gsa Today 28 (12), 4–9.
Karlsen, K.S., Conrad, C.P., Magni, V., 2019. Deep water cycling and sea level change since the breakup of Pangea. Geochem., Geophys., Geosys. 20 (6), 2919–2935.
Karlsen, K. S., M. Domeier, C. Gaina, and C. P. Conrad (2020), A tracer-based algorithm for automatic generation of seafloor age grids from plate tectonic reconstructions, Comput. Geosci., 140, 104508, doi:https://doi.org/10.1016/j.cageo.2020.104508.
Kocsis, Á.T., Scotese, C.R., 2021. Mapping paleocoastlines and continental flooding during the Phanerozoic. Earth-Science Reviews 213, 103463. https://doi.org/10.1016/j.earscirev.2020.103463.
Kominz, M.A., Miller, K.G., Browning, J.V., Katz, M.E., Mountain, G.S., 2016. Miocene relative sea level on the New Jersey shallow continental shelf and coastal plain derived from one-dimensional backstripping: A case for both eustasy and epeirogeny. Geosphere 12 (5), 1437–1456.
Lambeck, K., Rouby, H., Purcell, A., Sun, Y., Sambridge, M., 2014. Sea level and global ice volumes from the Last Glacial Maximum to the Holocene. PNAS 111 (43), 15296–15303. https://doi.org/10.1073/pnas.1411762111.
Lithgow-Bertelloni, C., Silver, P.G., 1998. Dynamic topography, plate driving forces and the African superswell. Nature 395 (6699), 269–272.
Marcilly, C.M., Torsvik, T.H., Domeier, M., Royer, D.L., 2021. New paleogeographic and degassing parameters for long-term carbon cycle models. Gondwana Research 97, 176–203. https://doi.org/10.1016/j.gr.2021.05.016.
Merdith, A.S., Williams, S.E., Collins, A.S., Tetley, M.G., Mulder, J.A., Blades, M.L., Young, A., Armistead, S.E., Cannon, J., Zahirovic, S., Müller, R.D., 2021. Extending full-plate tectonic models into deep time: Linking the Neoproterozoic and the Phanerozoic. Earth Sci. Rev. 214. https://doi.org/10.1016/j.earscirev.2020.103477.
Miller, K.G., Kominz, M.A., Browning, J.V., Wright, J.D., Mountain, G.S., Katz, M.E., Pekar, S.F., 2005. The Phanerozoic record of global sea level change. Science 310 (5752), 1293–1298.
Mills, B., Daines, S.J., Lenton, T.M., 2014. Changing tectonic controls on the long-term carbon cycle from Mesozoic to present. Geochem., Geophys., Geosys. 15 (12), 4866–4884.
Montañez, I.P., Poulsen, C.J., 2013. The Late Paleozoic Ice Age: An Evolving Paradigm. Annu. Rev. Earth Pl. Sc. 41 (1), 629–656.
Moucha, R., Forte, A.M., Mitrovica, J.X., Rowley, D.B., Quere, S., Simmons, N.A., Grand, S.P., 2008. Dynamic topography and long-term sea level variations: There is no such thing as a stable continental platform. Earth Planet. Sci. Lett. 271 (1–4), 101–108. https://doi.org/10.1016/j.epsl.2008.03.056.
Müller, R.D., Sdrolias, M., Gaina, C., Steinberger, B., Heine, C., 2008. Long-term sea level fluctuations driven by ocean basin dynamics. Science 319 (5868), 1357–1362.
Pitman, W.C., 1978. relationship between eustacy and stratigraphic sequences of passive margins. Geol. Soc. Am. Bull. 89 (9), 1389–1403.
Rocha-Campos, A.C., dos Santos, P.R., Canuto, J.R., Fielding, C.R., 2008. Late paleozoic glacial deposits of Brazil: Paraná Basin. Resolving the late Paleozoic ice age in time and space: GSA Special Paper 441, 97–114.
Ronov, A.B., 1994. Phanerozoic transgressions and regressions on the continents; a quantitative approach based on areas flooded by the sea and areas of marine and continental deposition. Am. J. Sci. 294 (7), 777–801.
Scotese, C. R. (2016). PALEOMAP PaleoAtlas for GPlates and the PaleoData Plotter Program PALEOMAP Project (2016)(http://www.earthbyte.org/paleomap-paleoatlas-for-gplates/)
Scotese, C.R., Golonka, J., 1992. Paleogeographic atlas: Paleomap Project. Texas, Department of Geology, University of Texas at Arlington, Arlington.
Scotese, C.R., Song, H., Mills, B.J., van der Meer, D.G., 2021. Phanerozoic paleotemperatures: The earth's changing climate during the last 540 million years. Earth-Sci.Rev. 215, 103503.
Snedden, J.W., Liu, C., 2010. A Compilation of Phanerozoic Sea level Change. Coastal Onlaps and Recommended Sequence Designations. Search Discov, Artic.
Snedden, J.W., Liu, C., 2011. Recommendations for a uniform chronostratigraphic designation system for Phanerozoic depositional sequences. AAPG Bull. 95 (7), 1095–1122. https://doi.org/10.1306/01031110138.
Smith, A.G., Smith, D.G., Funnell, B.M., 2004. Atlas of Mesozoic and Cenozoic coastlines. Cambridge University Press.
Soreghan, G.S., Soreghan, M.J., Heavens, N.G., 2019. Explosive volcanism as a key driver of the late Paleozoic ice age. Geology 47 (7), 600–604.
Spasojevic, S., Liu, L., Gurnis, M., Müller, R.D., 2008. The case for dynamic subsidence of the US east coast since the Eocene. Geophysical Research Letters 35 (8), L08305. https://doi.org/10.1029/2008GL033511.
Spasojevic, S., Gurnis, M., 2012. Sea level and vertical motion of continents from dynamic earth models since the Late Cretaceous. AAPG bulletin 96 (11), 2037–2064.
Stampfli, G.M., Hochard, C., Vérard, C., Wilhem, C., vonRaumer, J., 2013. The formation of Pangea. Tectonophysics 593, 1–19.
Svensen, H.H., Torsvik, T.H., Callegaro, S., Augland, L., Heimdal, T.H., Jerram, D.A., Planke, S., Pereira, E., 2018. Gondwana Large Igneous Provinces: plate reconstructions, volcanic basins and sill volumes. Geological Society, London, Special Publications 463 (1), 17–40.
Sømme, T.O., Helland-Hansen, W., Granjeon, D., 2009. Impact of eustatic amplitude variations on shelf morphology, sediment dispersal, and sequence stratigraphic interpretation: Icehouse versus greenhouse systems. Geology 37 (7), 587–590.
Torsvik, T.H., Rousse, S., Labails, C., Smethurst, M.A., 2009. A new scheme for the opening of the South Atlantic Ocean and dissection of an Aptian Salt Basin. Geophysical Journal International 177, 1315–1333.
Torsvik, T.H., Steinberger, B., Gurnis, M., Gaina, C., 2010a. Plate tectonics and net lithosphere rotation over the past 150 My. Earth and Planet. Science Letters 291 (1-4), 106–112.
Torsvik, T.H., Burke, K., Steinberger, B., Webb, S.J., Ashwal, L.D., 2010b. Diamonds sampled by plumes from the core–mantle boundary. Nature 466 (7304), 352–355. https://doi.org/10.1038/nature09216.
Torsvik, T.H., van der Voo, R., Doubrovine, P.V., Burke, K., Steinberger, B., Ashwal, L. D., Trønnes, R.G., Webb, S.J., Bull, A.L., 2014. Deep mantle structure as a reference frame for movements in and on the Earth. PNAS 111 (24), 8735–8740.
Torsvik, T.H., Steinberger, B., Ashwal, L.D., Doubrovine, P.V., Trønnes, R.G., Polat, A., 2016. Earth Evolution and Dynamics – A tribute to Kevin Burke. Can. J. of Earth Sci. 53 (11), 1073–1087. https://doi.org/10.1139/cjes-2015-0228.
Torsvik, T.H., Cocks, L.R.M., 2017. Earth History and Palaeogeography. Cambridge University Press, p. 317 pp..
Torsvik, T. H., Svensen, H. H., Steinberger, B., Royer, D. L., Jerram, D. A., Jones, M. T., & Domeier, M. (2021). Connecting the deep Earth and the atmosphere. *In* Mantle Convection and Surface Expressions (Edited by Hauke Marquardt, Maxim Ballmer, Sanne Cottaar and Jasper Konter). Geophysical Monograph 263, 413-453. American Geophysical Union. DOI: 10.1002/9781119528609.ch16.
Vail, P. R., Mitchum Jr, R. M., & Thompson III, S. (1977). Seismic stratigraphy and global changes of sea level: Part 4. Global cycles of relative changes of sea level.: Section 2. Application of seismic reflection configuration to stratigraphic interpretation.
van der Meer, D.G., van den Berg van Saparoea, A.P.H., van Hinsbergen, D.J.J., van de Weg, R.M.B., Godderis, Y., Le Hir, G., Donnadieu, Y., 2017. Reconstructing first-order changes in sea level during the Phanerozoic and Neoproterozoic using strontium isotopes. Gond. Res. 44, 22–34.
Vérard, C., Hochard, C., Baumgartner, P.O., Stampfli, G.M., Liu, M., 2015. 3D palaeogeographic reconstructions of the Phanerozoic versus sea-level and Sr-ratio variations. J. Palaeogeogr. 4 (1), 64–84.
Vérard, C., 2017. Statistics of the Earth's Topography. Open Access Library Journal 04 (06), 1–50.
Veevers, J.J., 2004. Gondwanaland from 650–500 Ma assembly through 320 Ma merger in Pangea to 185–100 Ma breakup: supercontinental tectonics via stratigraphy and radiometric dating. Earth-Sci. Rev. 68 (1-2), 1–132.
Walker, L.J., Wilkinson, B.H., Ivany, L.C., 2002. Continental drift and Phanerozoic carbonate accumulation in shallow-shelf and deep-marine settings. J. Geol. 110 (1), 75–87.
Wright, N.M., Seton, M., Williams, S.E., Whittaker, J.M., Müller, R.D., 2020. Sea level fluctuations driven by changes in global ocean basin volume following supercontinent break-up. Earth Sci. Rev. 208, 103293. https://doi.org/10.1016/j.earscirev.2020.103293.
Zhang, Y., 2005. Global tectonic and climatic control of mean elevation of continents, and Phanerozoic sea level change. Earth Planet. Sci. Lett. 237 (3-4), 524–531.